Effect of different synthesis methods on the morphology, optical behavior, and superior photocatalytic performances of Ag$_3$PO$_4$ sub-microcrystals using white-light-emitting diodes

J.F. Cruz-Filho[a], T.M.S. Costa[a], M.S. Lima[a], L.J. Silva[b], R.S. Santos[a], L.S. Cavalcante[a], E. Longo[c], G.E. Luz Jr.[a],*

[a] PPGQ-GERATEC, Universidade Estadual do Piauí, Rua: João Cabral, N. 2231, P.O. Box 381, 64002-150, Teresina, PI, Brazil
[b] Departamento de Química-DQ-PPGQ, Universidade Federal do Piauí–UFPI, Petrônio Portela, 64049-550, Teresina, PI, Brazil
[c] Departamento de Físico-Química, Universidade Estadual Paulista, 14800-060, Araraquara, SP, Brazil

ARTICLE INFO

ABSTRACT

In this paper, we report on the superior photocatalytic properties of silver orthophosphate (Ag$_3$PO$_4$) sub-microcrystals prepared using different synthesis methods: precipitation (PM), precipitation-calcination (PM-C), and precipitation-hydrothermal (PM-H), on the degradation of Rhodamine B (RhB) cationic dye and methyl orange (MO) anionic dye using white-light-emitting diodes (WLEDs). The structure of the Ag$_3$PO$_4$ sub-microcrystals obtained was investigated by X-ray diffraction (XRD), Rietveld refinement, micro-Raman (M-Raman), and Fourier transform infrared (FT-IR) spectroscopy. The X-ray photoelectron spectroscopy (XPS) was used to investigate the surface chemical composition and states. The shape, average crystal size, and morphological changes were observed using field emission scanning electron microscopy (FE-SEM). The results indicated that all samples have cubic body-centered, P $\bar{4}$3 n (218) space group, with the following crytallite size: PM (103.4 nm), PM-C (56.7 nm) and PM-H (123.8 nm). Also, it was observed the optical band gap values of 2.23, 2.15 and 2.16 eV of the samples PM, PM-C and PM-H, respectively. For both dyes, the PM-C sample has higher photodegradation efficiency (98%) and apparent quantum efficiency ($\varphi_x = 0.081$) in relation to PM and PM-H samples. In addition, especially to RhB, the apparent quantum efficiency of samples practically remains unchanged by three photocatalytic cycles due to use of white light emitting diode (WLEDs) illumination.

1. Introduction

The general formula for metal phosphates or metal orthophosphates can be written as A_3PO$_4$, where A is a monovalent (A^+ = Li, Na, K, or Rb)*s*-alkaline metal, Cu, or Ag [1–3]. A literature survey revealed that among these phosphates, silver phosphate (Ag$_3$PO$_4$), a yellow precipitate insoluble in aqueous solutions, has been studied the most [4]. The simplest, most common synthesis method for Ag$_3$PO$_4$ is the precipitation reaction between silver nitrate (AgNO$_3$) and dibasic sodium phosphate dodecahydrate (Na$_2$HPO$_4$·12H$_2$O) or tribasic sodium phosphate (Na$_3$PO$_4$) [5]. Ag$_3$PO$_4$ may form crystals with different shapes, which sensibly depend on the method of preparation, capping agent [6], surfactant [7], pH conditions [8], and solvent [9], which can change the direction of growth and produce different crystalline structures [10–13]. The electronic structure of the Ag$_3$PO$_4$ crystals is cubic with $P\bar{4}3n$) space group, T_d symmetry point group, and two molecular formula units per unit cell (Z = 2) [14]. The unit cells exhibit the same chemical coordination (equal to four), but are formed by highly distorted tetrahedral [AgO$_4$] clusters and undistorted tetrahedral [PO$_4$] clusters [15].

The increasing degradation of natural resources due to anthropic action has reached catastrophic dimensions, and this can be observed through alterations in the environment. Thus, the monitoring and mitigation of polluting industrial waste emissions have become urgent [16,17].

In this context, the treatment of effluents using adsorption [18,19] and catalytic processes [20,21] was studied and employed. Among the processes studied, advanced oxidative processes (OAPs) are currently attracting the interest of several research groups, since they have the advantage of degradation of several persistent organic compounds, without the use of other potentially contaminating oxidants. [22–24].

Among AOPs, heterogeneous photocatalysis has been gaining

---

prominence since 1972, and has become an alternative for solving energy and environmental problems [25]. Due to the pioneering work by Asahi et al. [26] and Zou et al. [27], new advances have been made not only to improve the quantum efficiency of photocatalysts under visible light but also to develop new semiconductor materials with desired energy bands for efficiently converting photons to electrons [28–30].

Semiconductors are good alternatives as photocatalysts in the field of environmental engineering, and can also be used to produce and store energy [31–33]. For these purposes, there are three characteristics that are wish for a semiconductor: high efficiency in the separation of electron/hole (e^-/h^+) pairs under light radiation, low recombination ratio of electron/hole (e^-/h^+), and high visible light absorption [34–36].

In this context, Ag_3PO_4 crystals have demonstrated a good photocatalytic performance, as well as an indirect band gap of ≅2.36 eV and 2.43 eV for direct band gap, ideal for the absorption of visible light with wavelength ≤ 530 nm [13,37]. It should be noted that the band gap values of Ag_3PO_4 tend to increase with the reduction of particle size [38], as well as the wavelength range in which it absorbs varies with the morphology [10,13].

The oxidation-reduction capacity of Ag_3PO_4 when irradiated under a specific wavelength is due to its maximum valence band (MVB) of 2.67 V over the standard hydrogen electrode (SHE), which is greater than the potential of reduction of water (= 1.23 V), which justifies the formation of O_2 from water; However, since the minimum conduction band (MCD) of 0.24 V is greater than the reduction potential of the $2H^+ / H_2$ pair (= 0.008), Ag_3PO_4 is not able to reduce water to obtain H_2 [37].

The photocatalytic property of this semiconductor is due to its electronic structure, since its valence band (VB) is constitued by states (2p) of the oxygen and (4d) of the silver. While, the conduction band (CB) presents the states (5 s and 5p) of the silver, which are hybridized, causing energy dispersion and favoring the transfer of the electrons to the surface in all directions [39–41].

The presence of "d states" in the conduction band hinders the mobility of the electrons, favoring the recombination of the pair e^-/h^+, which suggests reduction of the photocatalytic activity. However, the ions $3Ag^+$ and PO_4^{3-} present in the crystalline lattice inhibit the effect of the d orbitals on the CB of Ag_3PO_4, contributing to the separation of the Ag (5 s) orbitals present in the CB of Ag(4d) and O (2p) found in VB. Thus, the high photocatalytic performance of Ag_3PO_4 can also be attributed to the absence of character d in BC [110].

Although the Ag_3PO_4 presents excellent photocatalytic performance, the main obstacles for its practical applications are the photocorrosion during the photocatalytic process. and loss of photocatalytic efficiency due to inactivation due to the formation of Ag° particles on the surface of the photocatalyst [37].

Recently, some studies have demonstrated that the crystal size and morphology [38,42,43], presence of certain crystalline faces [8,12,13,44], effect of the localized surface plasmon resonance (LSPR) induced by metallic Ag nanoparticles [44–46],synthesis methods [5,47–49], and use of blue light emission diodes (LEDs) as radiation sources [50] directly influence the photocatalytic performance of Ag_3PO_4.

Since the emergence of blue LED based on AlInGaN and subsequently the development of high gloss white-light-emitting diodes (WLEDs) in 1996 by Nakamura and Fard [51,52], these devices have been attracting the interest of researchers due to the possibility of developing compact photocatalytic reactors using energy-efficient, relatively long life expectancy, flexible, improved luminous intensity, and easily adjustable emission wavelength luminous devices [53,54].

Therefore, in this paper, we reported the effects of different synthesis methods (precipitation, precipitation-calcination, and precipitation-hydrothermal) for obtaining Ag_3PO_4 sub-microcrystals with photocatalytic properties using WLEDs. Moreover, we investigated the structure of the obtained Ag_3PO_4 sub-microcrystals using X-ray

diffraction (XRD), Rietveld refinement, and micro-Raman (M-Raman) and Fourier-transform infrared (FT-IR) spectroscopy. The optical behavior of the Ag_3PO_4microcrystals was analyzed using UV–vis diffuse reflectance spectroscopy. Finally, the superior photocatalytic properties of the Ag_3PO_4 microcrystals prepared using different synthesis methods were analyzed for fast degradation of Rhodamine B (RhB) cationic dye and methyl orange (MO) anionic dye using an InGaN-based WLED with incorporated Phosphor (λ = 645–430 nm) [55] for the first time.

2. Experimental section

2.1. Materials

Silver nitrate ($AgNO_3$), sodium hydrogen phosphate (Na_2HPO_4), RhB (95% purity), and MO (85% purity) were purchased from Sigma-Aldrich. Deionized water was obtained using a Purelab Option-Q Elga model DV-25 deionizer. All reagents used in this study were of analytical grade. The Ag_3PO_4 sample was prepared using the precipitation method. Thus, 76.4 mg $AgNO_3$ and 21.3 mg Na_2HPO_4 were dissolved in 3 and 1 mL deionized water, respectively. The solutions were sonicated for 10 min and gradually diluted using deionized water to a volume of 500 mL. The solution was protected from ambient light. It should be noted that the temperature varied naturally from 4 to 18 °C, while the pH remained approximately 6.5. After 72 h, the precipitate powder was oven-dried at 60 °C for 3 h. The sample thus synthesized was called PM. An aliquot of the PM sample was thermally treated in a muffle furnace at 150 °C for 6 h, without air flow. Hereafter, this sample is referred to as the PM-C sample. Another aliquot was hydrothermally treated. Thus, 0.2 g of the PM sample was dispersed in 100 mL deionized water, transferred to a Teflon beaker, and autoclaved in a stainless-steel reactor at 150 °C for 6 h. The powder was subsequently centrifuged, separated and dried at 60 °C for 3 h. This sample is here after referred to as the PM-H sample. All synthesized powders were stored in appropriate amber vials.

2.2. Materials characterization

The diffraction patterns were obtained in the 2θ range of 10–110° with a step of 0.02°, time of 1 s, and a scanning rate of 1°min^{-1}. Structural and microstructural analyses of the XRD data were performed using Rietveld refinement utilizing the Toolbar software FullProf Suite Program©version 3.00. The Bragg peak profile was modeled using the modified Thompson–Cox–Hastings pseudo-Voigt convolution with axial divergence asymmetry (TCHZ-pV). The angular dependence of the peak shape and full width half maximum (FWHM) were defined using the function determined by Caglioti, Paoletti and Ricci [56]. The instrument contribution to the width of each peak was estimated and subtracted by obtaining the *U, V, W, X,* and *Y* parameters using the Rietveld refinement of the XDR standard CeO_2 sample [57]. The anisotropic microstructural effect was treated using the Voigt approximation based on the Gaussian and Lorentzian contributions to the profile of the diffraction peak, and the anisotropic size enlargement was described in terms of a linear spherical harmonic combination of the refractable coefficients corresponding to the m $\bar{3}$ m class of Laue [58]. The apparent "shape" of the crystallite was obtained using Gfourier©, a program available in the Fullprof software package. The Williamson-Hall (W-H) method was used to explain the effect of size and microstrain on the amplification of the diffraction peak and the effects of anisotropic deformation were considered using Stephen's formalism [59].

Raman spectra were obtained using a Bruker model SENTERRA device in the 200–1200 cm^{-1}spectral region with an automatic resolution of 3 cm^{-1} and laser with an output power of 5 mW and a wavelength of 532 nm. The device was also equipped with an Olympus BX50 microscope. We obtained the FTIR spectra by applying the dilution method to KBr pellets in the 400–4000 cm^{-1} range, using a

Shimadzu IR Prestige-21 spectrometer with a resolution of 4 cm^{-1}. In addition, FE-SEM was performed using a FEI brand, Quanta FEG model field emission electron source. The morphology of the synthesized powders and the distribution of the particle size obtained using the graphical editor Gimp$^{©}$ version 2.8.16 were estimated from the micrographs.

The spectra of the X-ray photoelectron spectroscopy (XPS) were obtained using ThermoFisher Scientific™ model K-alpha™ with Al Kα1 X-ray (hν = 1486.6 Ev) radiation source.

Finally, UV–vis spectroscopy was performed using a model UV-2600 Shimadzu spectrophotometer in the 200–800 nm wavelength range to obtain diffuse reflectance spectra. The obtained results were used to estimate the bandwidth energy values by applying the Kubelka-Munk functions [60].

2.3. Photocatalytic activity evaluation

The photocatalytic performance of the PM, PM-C, and PM-H powders were individually evaluated for the degradation of RhB and MO dyes in 10 mgL^{-1} aqueous solutions. For each catalytic assay, 25 mg of the synthesized powder was dispersed in 25 mL RhB dye solution and kept under magnetic stirring at 30 °C in a glass cell 6 cm from the irradiation source.

The photocatalytic reactor for the degradation reaction consisted of an arrangement of WLEDs with a luminous flux (Φv) of 85 l m and relative power density of 15 mW m^{-2} (Fig. S1). Before irradiation, the suspension was kept for 30 min in the dark under magnetic stirring to establish the adsorption/desorption equilibrium of the RhB dye on the surface of the catalysts. To analyze the degradation of RhB, 2 mL aliquots were collected and centrifuged at 6000 rpm for 10 min. The supernatant was analyzed using UV–vis spectroscopy. The same procedure was used for the degradation of the MO dye. The maximum wavelengths used to calculate the percent degradation of RhB and MO were 554 and 460 nm, respectively. The percentage rate of photodegradation of the RhB and MO dyes was calculated using Eq. (1):

$$Rate of photodegradation (\%) = \frac{C_0 - C}{C_0} \times 100 \qquad (1)$$

where C_0 is the initial concentration of the dye and C is the concentration measured at different times during irradiation.

2.4. Determination of photon flux and apparent quantum efficiency

To determine the photon flux and apparent quantum efficiency, 5 mL of a solution of potassium ferrioxalate at 0.15 mol L^{-1} were irradiated with WLED$_S$ (645–430 nm) for 120 s. Afterward, 1 mL of that solution was added to 4 mL of an aqueous solution of 1,10-phenanthroline at 0.2 mmol L^{-1} and rediluted with 20 mL deionized water. The procedure was performed in triplicate and the average absorbance of the Fe^{2+}/phenanthroline complex was obtained at 510 nm. The apparent quantum efficiencies of the photocatalysts were calculated assuming that the degradations of RhB and MO chromophores absorbing at 554 and 460 nm, respectively, were one e$^-$/h$^+$ processes (which was, of course, not true, since the number of e$^-$/h$^+$ pairs participating in dye degradation was much higher in reality) [61,62].

3. Results and discussion

3.1. Characterization results

The XRD patterns of the (a) PM, (b) PM-C, and (c) PM-H samples shown in Fig. 1 demonstrate the presence of characteristic peaks for the cubic crystal phase of Ag$_3$PO$_4$ indexed by the Inorganic Crystal Structure Database (ICSD) N° 200 972 crystallographic pattern [63].

In addition, using the (210) diffraction plane as reference, it can be observed (inset of Fig. 1) that the diffractogram of the PM-C sample
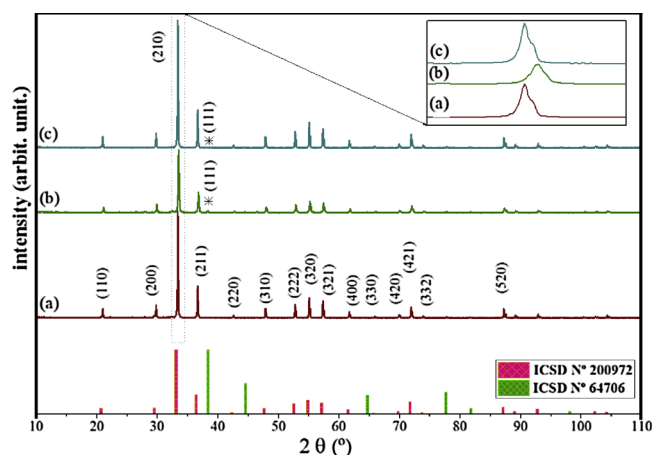

Fig. 1. X-ray diffraction patterns of samples: (a) PM, (b) PM-C and (c) PM-H. (d) ICSD N° 200,972 and 64,706. Insert: displacement and enlargement of the diffraction peak at high angle 2θ having as reference the diffraction peak of the plane (210).

undergoes displacement and broadening of all diffraction peaks at high 2θ angles. This phenomenon can be attributed to the reduction of the interplanar distance initially provoked by the non-uniform plastic deformation the PM-C sample underwent during calcination [64,65].

Furthermore, a discrete peak 2θ = 38° (*) indexed to the (111) plane of metallic Ag (ICSD N° 64706) was observed in the XRD patterns of the PM-C and PM-H samples.

The Rietveld refinement compliance constants of the patterns of the PM, PM-C, and PM-H samples shown in Fig. 2a were associated with the following reliability indices: profile factor (R$_p$), weighted profile factor (R$_{wp}$), expected weighted profile factor (R$_{exp}$), Bragg factor (R$_{Bragg}$), and adjustment factor (χ^2), as shown in Table 1. These data suggest that the refined samples have a cubic body centered structure and P$\overline{4}$3n (218) spatial group, indexed in compliance with ICSD N° 200 972. Using the atomic positions derived from the refinement data (Tab. S1), the unit cell shown in Fig. 2b was modeled using the Vesta$^{©}$ software version 3.3.2 [66]. In this modeled structure, the Ag and P atoms are coordinated with four O atoms, resulting in tetrahedral [AgO$_4$] and [PO$_4$] clusters. Each [PO$_4$] cluster has in its vicinity three [AgO$_4$] agglomerates bound by O atoms. The existence of two binding angles (α and β) indicated that the [AgO$_4$] agglomerates are highly distorted in the network, because of the inductive effect caused by the high electronegativity of the clusters [15,67]. There were no significant variations in the angles and bond lengths of the analyzed samples.

When the synthesized materials are prone to imperfect crystallization, combining the Rietveld method with the profile shape model of the diffraction peak is extremely useful. The study of structural imperfections using average values of powder diffraction is known as line profile analysis or microstructural analysis [68]. This technique is based on the analysis of the deviation of the crystallinity of polycrystalline materials, generated by the influence of crystallite size, strain, and microstrain of the crystalline lattice on the profile of the diffractogram [69–71].

The W-H method proposed in 1953 involves constructing a graph that allows the separation of the contributions of the average crystal size and microstrain extracted from the analysis of the diffraction profile, considering as order of reflection [69]. This method is a graphical representation of β cos(θ)/λ as a function of sin(θ)/λ. After plotting the points, linear regression is used to obtain the apparent size of the crystallite from the y intercept, while the apparent deformation of the network, η (network microstrain), is extracted from the slope of the line. When η = 4. < ε > is referred to as the apparent microstrain of Stokes [72].

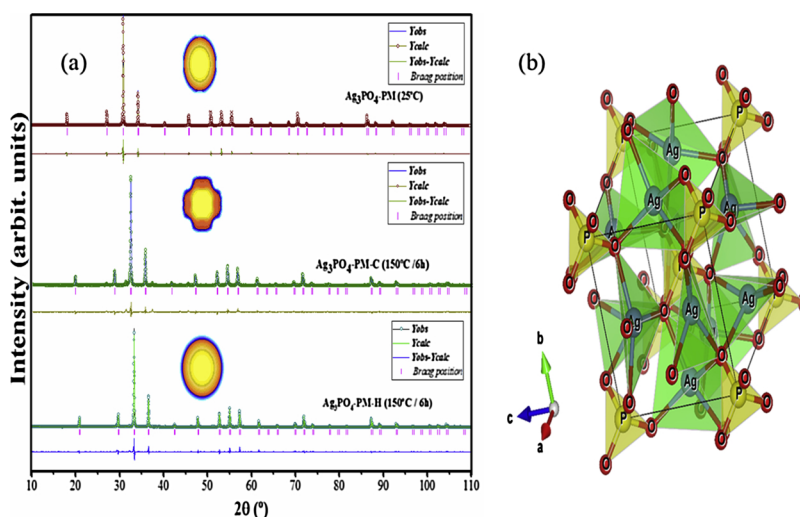In Fig. 3a and b obtained using the W-H method demonstrates that

Fig. 2. (a) Rietveld refinement using an anisotropic model and apparent crystallite size form (insert of the Figures) obtained from the refinement of the spherical harmonic coefficients of the XRD patterns of samples: PM, PM-C and PM-H. (b) modeling of cell unit Ag_3PO_4 crystals.

Table 1

Rietveld refinement parameters PM, PM-C and PM-H samples and parameters indexed in the catalog database.

Sample	Cell Parameters (Å) $(a = b = c)$	Quality Indices					
		*R_p	*R_{wp}	*R_{exp}	*χ^2	*R_B	Cell volume (Å^3)
PM	6.011(5)	10.5	13.4	10.41	1.66	4.87	217.24
PM-C	6.013(5)	12.5	12.5	10.31	1.00	3.90	217.45
PM-H	6.011(2)	10.7	13.2	9.92	1.77	4.24	217.20
ICSD Nº 200,972	6.009(6)	–	–	–	–	–	217.03

*R_p = profile factor; *R_{wp} = weighted profile factor; *R_{exp} = expected weighted profile factor; *R_{braag} = Bragg factor and χ^2 (adjustment factor).

the PM and PM-C samples show a significant degree of dispersion for the points around the linear fit compared to those of the PM-H samples (Fig. 3c) and qualitatively suggest the presence of a high degree of

voltage anisotropy [73]. This effect is related to the broadening of the diffraction peak caused by the microstrain, which is in agreement with the fundamental dispersion theory, since it is expected that the size of the contribution of the microstrain to the enlargement of the peak will be uniform, while the contribution of the increase in the microstrain is directly proportional to the reciprocal space [74].

The positive slope of the linear adjustment suggests that the diffraction peak broadening is related to the prevalence of the microstrain effect on the crystallite size [75].

Sample PM-H (Fig. 3c) shows a better fit of the dispersion of the points around the linear fit. This demonstrates that the *hkl*-anisotropic effects are slightly more discrete compared to those of the PM and PM-C samples. Thus, it was expected that the diameter of the crystallites was approximately the same in all *hkl*-anisotropic directions and consequently the sample had spherical morphology [76].

The apparent crystallite size distribution of the PM-C, PM, and PM-H samples was obtained at the end of the Rietveld refinement (Fig. 2)
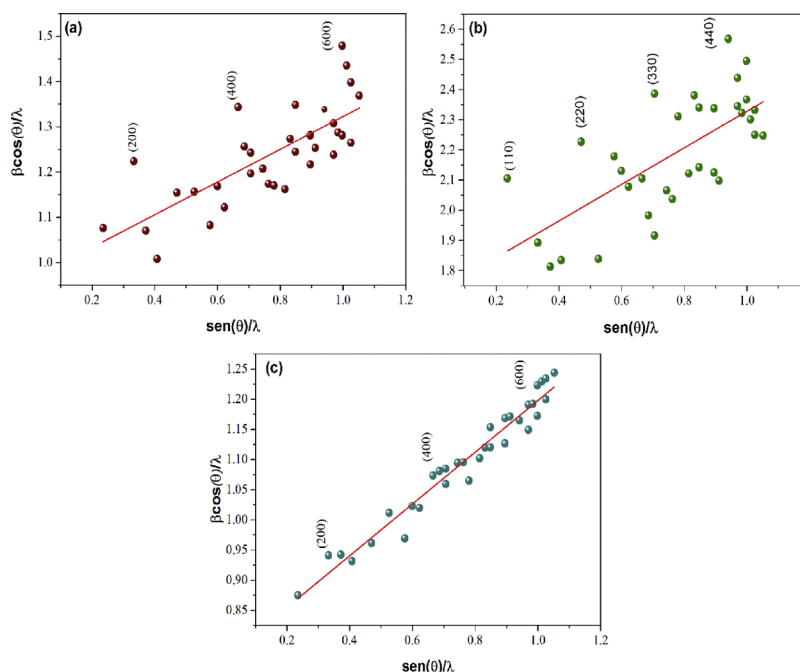

Fig. 3. Graphical representation of the Williansom-Hall method for the analyzed samples: (a) PM, (b) PM-C and PM-H (c).

associated with the use of linear combinations of spherical harmonics for the amplification of the diffraction peak from the anisotropic Lorentzian size expansion effect. This effect demonstrated the distribution of the apparent size in relation to each reciprocal network vector (Table S2) [77,78].

It was possible to obtain the distribution graph of the apparent crystallite size (inset of Fig. 2a–c) from the refinement of the spherical harmonic coefficients, using the Gfourier© software, version 04.06. The overall apparent average crystallite sizes of the PM, PM-C, and PM-H samples were 103.4, 56.7, and 123.8 nm, respectively.

The PM-C sample showed a significant increase in network microstrain (η = 6.03) compared to those of the PM (η = 2.07) and PM-H (η = 1.4) samples in the contact region between particles during the sintering of the material. This increase was facilitated by line defects (dislocations) [79,80]. During calcination, the decrease in the crystallite size induced by the diffusion of matter and vacancies through the bulk and the contours of the contact zone of the particles justified the contraction of the structure at a given temperature [81,82]. For the PM-H sample, the increase in crystallite size and reduction in η was influenced by the dissolution and recrystallization of the sample during the hydrothermal process leading to highly crystalline materials due to more energetic conditions [83].

Quantitative analysis was performed using diffraction profile analysis, proposed by Hugo M. Rietveld, is widely accepted and has as main advantage to minimize or eliminate inaccuracies due to preferential orientation, microabsorption, diffraction peak overlap and detection of amorphous phases or phase traces present in the sample [84,85]. However, there are two preconditions to be followed: (i) the quantified phase is the crystalline phase and (ii) the crystalline structure is known [86].

The diffraction profiles of the samples analyzed quantitatively by the Rietveld method (Fig. S2) demonstrated the massive proportion of (1.8%) Ag° in the sample PM-C and (0.8%) for the PM-H sample. The presence of the Ag° phase is due to the thermal and hydrothermal treatments in which the samples were submitted respectively [48,87]. Although, the quantitative refinement by the Rietveld method shows that the presence of Ag° for the sample PM-C and PM-H is below the detection limit for the XRD technique (~5 mol%) [88].

However, it is important to note that the quantitative method using the Rietveld method presented values close to that reported in the literature for the sample PM-C in the range of 100–200 °C [89]. As shown in Fig. 1, it was not possible to observe diffraction spikes for the planes of metallic Ag in the PM sample.

Raman spectra are shown in Fig. 4, where eight active vibrational modes characteristic of the phosphate group [PO$_4$] can be observed. The intense narrow band at 909 cm^{-1} is attributed to the symmetrical terminal oxygen stretch of the [PO$_4$] clusters, and the low intensity bands at 953 and 1001 cm^{-1} are related to the asymmetric stretches of the [PO$_4$] cluster. Moreover, broad bands at 409 and 542 cm^{-1} corresponding to the flexion of the [PO$_4$] cluster were

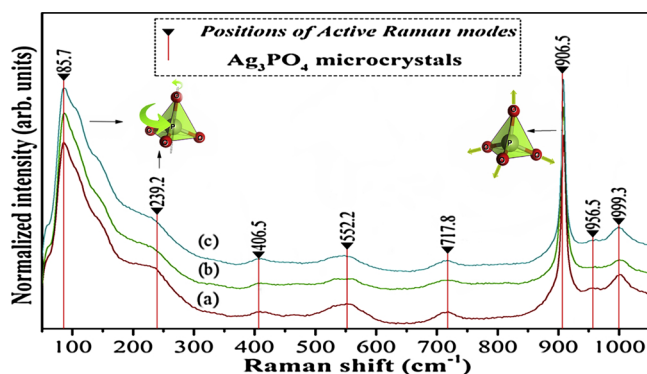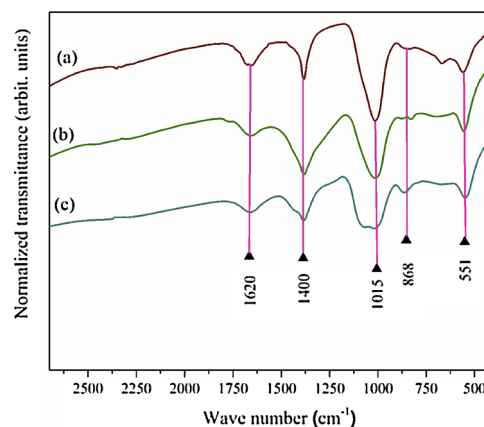**Fig. 5.** FTIR spectra of PM (a), PM-C (b) and PM-H (b) samples.

observed. Lastly, the band at 712 cm^{-1} was attributed to the symmetrical stretching of the P—O—P bonds [90].

From the FTIR spectra in Fig. 5, it can be observed that the samples synthesized in this study have characteristic bands at 1620 cm^{-1} that are attributed to the asymmetric stretch of the OH bond of the water molecules. In addition, the 551 cm^{-1} band represents the asymmetrical and symmetrical stretching of the O=P—O bonds [91]. Moreover, three lower-intensity bands at approximately 868, 1015, and 1400 cm^{-1} were observed. The first two bands can be attributed to the symmetrical and asymmetric stretching of the O—P—O bonds, respectively, and the last one to the vibrational stretching of the double bond of the P=O group [92,93].

The size and morphology of the Ag$_3$PO$_4$ samples were investigated using FE-SEM, and the results are shown in Fig. 6.

From Fig. 6a, it can be observed that the PM sample predominantly consists of cubic particles, although rhombic dodecahedral particles can also be observed. In addition, the average particle size in this sample was approximately 500 ± 97 nm (inset of Fig. 6a).

The micrograph of the PM-C sample in Fig. 6b shows sintered particles formed due to thermal treatment at 150 °C for 6 h, which may have induced the diffusion mechanism among particles causing the sintering of the material [64,65], as already mentioned when discussing the structure of the synthesized samples.

The hydrothermal treatment for the PM-H sample promoted a change in the structure of the particles, as seen in Fig. 6c. This sample shows spherical particles with an average particle size of approximately 526 ± 110 nm (inset of Fig. 6c).The spherical morphology may be related to the physical phenomenon known as the Ostwald growth, where particle growth is favored by the dissolution and recrystallization of the material tothe detriment of the smaller particles at a given temperature [94,95].

To determine the region of radiation absorption and the E$_g$ values of the samples, diffuse reflectance spectroscopy (DRS) in the UV–vis region was carried out.

From Fig. 7a, we can observe a similarity among the DRS spectra of the PM, PM-C, and PM-H samples, which absorb visible light with a wavelength smaller than 530 nm [8]. In addition, as shown in the quantitative method the rather low Ag^0 content in the PM, PM-C and PM-H samples did not exhibit significant increase in plasmonic absorption in UV–vis spectra around 340 nm [96].

Fig. 7b–d shows indirect E$_g$ for PM, PM-C, and PM-H samples. It can be observed that E$_g$ of the PM sample (2.23 eV) was slightly higher than those obtained for the PM-C (2.15 eV) and PM-H (2.16 eV) samples. The decrease in E$_g$ observed for the PM-C samples compared to that of the PM samples may be related to the structural deformations in the crystalline lattice, aside from the presence of oxygen vacancies [15,35,97]. The decrease in E$_g$ of the PM-H sample can be correlated with the increase in particle size observed after the hydrothermal treatment [5].

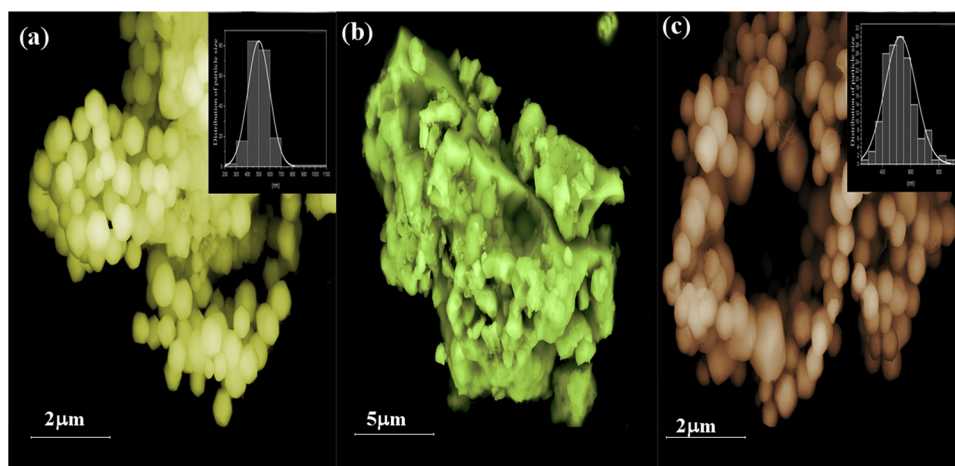**Fig. 4.** Raman spectra of PM (a), PM-C (b) and PM-H (b) samples.

Fig. 6. FE-SEM micrographs of samples (a) PM, (b) PM-C and (c) PM-H.

XPS spectra were employed to further analyze the surface crystal, elemental composition, chemical state, and electronic state. It can be seen from Fig. S3 that the XPS survey spectra with peak identification for all sample are similar, which contain the elements of Ag, P, O and C. According to Fig. 8(a−c), the high-resolution XPS spectra of the Ag 3d orbitals region show that synthesized samples consist of two characteristic peaks of the binding energies assigned to Ag 3d3/2 (~374 eV) and Ag 3d5/2, (~368 eV), respectively.

Due to the asymmetry of the profile of Ag 3d peaks, the deconvolution was employed and evidenced four contributions at 374.2, 375.4, 368.2 and 369.4 eV, respectively. The peaks at 375.4 and 369.4 eV can be attributed to the metal Ag^0, while the signals at 368.2 and 374.2 eV are related to the Ag^+ ions [98].

From relative peak area assigned to Ag^0 in Fig. 8, it was possible to observe that amount of Ag^0 dispersed on the PM-C surface (60%) is greater than that one on PM and PM-H samples (12% and 28%, respectively), which corroborates with results obtained by XDR and quantitative analysis at the Rietveld refinement, regarding the presence of metallic Ag on surface of these samples.

Fig. 9(a–c) show the high-resolution XPS spectra of O1s region of PM, PM-C and PM-H samples.

According to Fig. 9(a−c), the high-resolution XPS spectra of O1s orbitals region show the O1s peaks of all samples were decomposed into tree contributions at 530 (O_I), 531.3 (O_{II}) and 532.4 eV (O_{III}), respectively. The contribution O_I peak is attributed to the non-binding oxygen atoms of the group (P = 0). The peak O_{II} is associated with oxygen vacancies or defects on crystal lattice, which were occupied by O^{2-} ions before the heat treatment [98]. The contribution O_{III} is associated to oxygen and water molecules on the surface [98].

In Fig. 9, the relation between the peak area of O_{II} and the total area of all O1s peaks is 42%, 15% and 8% for PM-C, PM and PM-H samples, respectively. This indicates that the heat treatment promoted oxygen vacancies or defects on crystal lattice, like beforehand discussed in structural analysis from Rietveld method.

3.2. Photocatalytic activity

The photolysis results shown in Fig. 10(a) and (b) indicate that the RhB and MO dyes did not undergo degradation under WLED irradiation, suggesting that these compounds are highly stable [98,99].However, photocatalytic tests carried out in the presence of photocatalysts demonstrated the high efficiency of the samples for the degradation of MO and RhB dyes under WLEDs irradiation, as can be seen in Fig. 10(c) and (d). Moreover, it can be observed that both dyes photodegraded faster when using PM-C than when using PM-H or PM, the last one being the least efficient of the samples.

This behavior can be attributed to the presence of Ag^0 in the PM-C and PM-H samples, as already illustrated by the XRD patterns (Fig. 1) and demonstrated by the Rietveld quantitative refinement (Fig. S2) and XPS spectra (Fig. 8). It is known that the effect of high temperature sintering allows intimate contact not only between the semiconductor particles, but also between semiconductor particles and metal particles [100]. Proximity facilitates the migration of the photogenerated carriers between semiconductor particles, as well as between semiconductor and metallic particles. [100].

The contact between Ag_3PO_4/Ag relative to PM-C sample should be more compacted to PM-H. Thus, migration of the photogenerated carriers between Ag_3PO_4, Ag be easier in relation to sample PM-C and PM-H. Finally, the electrons occupied in the CB Ag_3PO_4 reduce further Ag^+ ions to metallic Ag° on the PM-C. This may be the other reason why high temperature calcination favors the formation of metallic Ag° in relation to sample PM-C.

In addition, the highest catalytic efficiency of the PM-C sample may also be related to the decrease in crystal size associated with the presence of microstrain, as presented in the microstructural analysis and the density of oxygen vacancies (Vös) on the surface of the material generated by sintering during the thermal treatment [101–103]. However, the same effect was not observed for the three catalytic cycles for the PM-H sample, since the hydrothermal synthesis method increased the size of crystallites and promoted the decrease in microstrain compared to those of the PM and PM-C samples, while possibly exerting a negative influence on the catalytic efficiency.

Therefore, the higher photocatalytic activity of the PM-C sample compared to those of the PM and PM-H samples is perhaps owing to the degree of defects produced during the thermal treatment, because photocatalytic activity is related to the diffusion of vacancies that increases the density of Vös on the surface of the catalyst [104,105]. Thus, the existence of surface defects can greatly influence the efficiency of e^-/h^+ separation, low recombination, and the corresponding photocatalytic activity. It is worth noting that mass defects can also be generated during the thermal treatment and could introduce electron capture sites and e^-/h^+ recombination, thus hindering the photocatalytic activity.

By contrast, surface and sub-surface defects, when overlap with the effect of mass defects, can contribute to e^-/h^+ separation, promoting the formation of available surface traps, making recombination difficult, facilitating the adsorption of the pollutant, and promoting an increase in photocatalytic activity [106–108].

It was observed that even when using photocatalysts, the degradation of MO was slower and/or less efficient than of that RhB. This can be related to the cationic nature of RhB and the anionic nature of MO, RhB being preferentially adsorbed onto the negatively charged surface
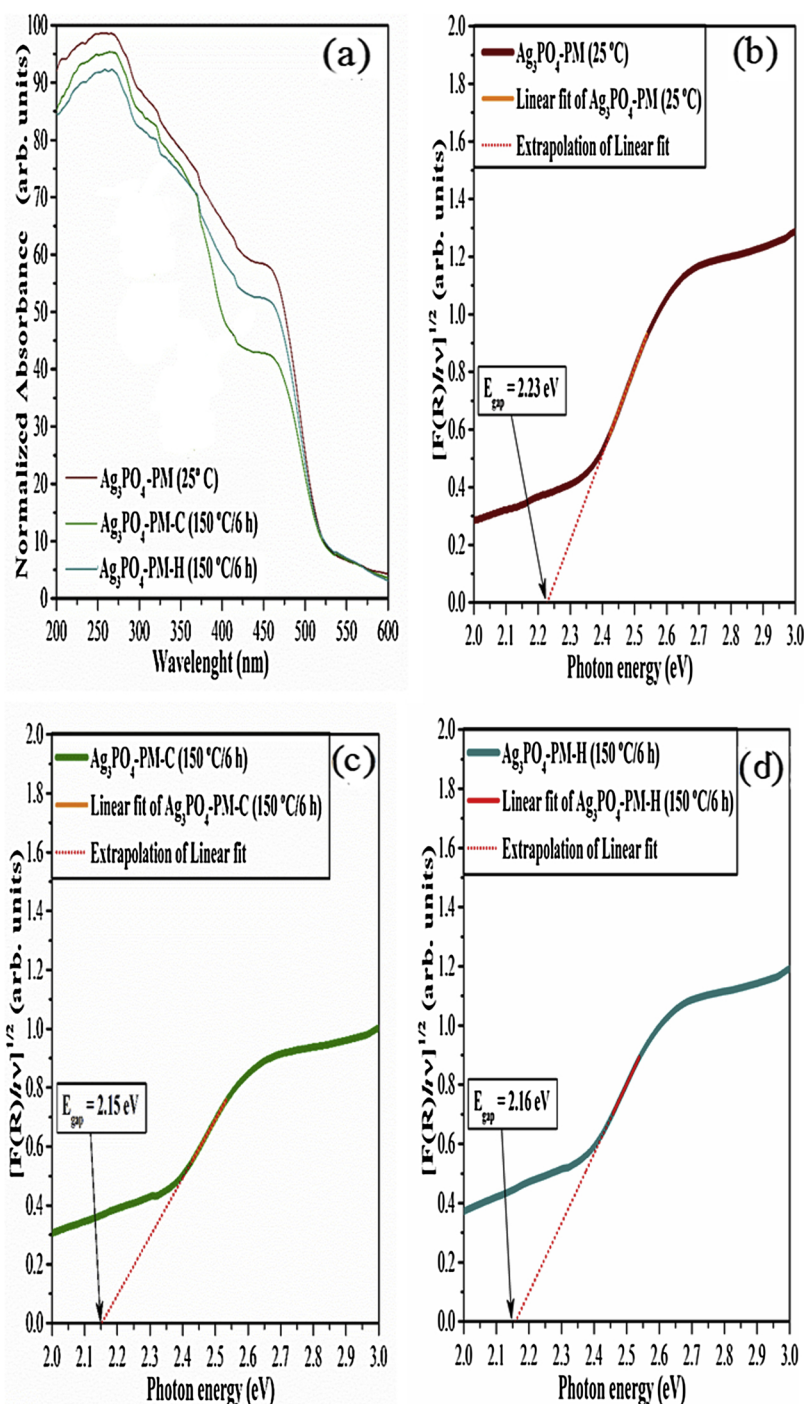
Fig. 7. UV–vis (a) and indirect band gap spectra obtained using the Kubelka-Munk method of the samples: (b) PM, (c) PM-C and (d). PM-H.

of the Ag_3PO_4 sub-microcrystals [89].

To evaluate the photochemical stability of the Ag_3PO_4 samples, we carried out three photocatalytic degradation cycles for MO and RhB for each sample under WLEDs irradiation. The results are shown in Fig. 11(a–c).

Further investigations were focused on exploring the stability of the Ag_3PO_4 samples for the degradation of MO and RhB dyes. As shown in Fig. 11a, a smooth and progressive reduction occurred in the photocatalytic performance of the PM-C and PM-H samples for the degradation of the MO dye during the three photocatalytic cycles. This can be related to the photoreduction of Ag^0 during the catalytic cycles [109].

As can be seen from Fig. 11, the photodegradation of MO was lower

than that of RhB. It is important to highlight that the wavelength range in the emission spectrum of the WLEDs capable of photoactivating Ag_3PO_4 (λ_{peak} = 460 nm) [55] and obtained experimentally (ESI Fig. S9.1), coincided with the absorption range of the chromophore groups present in the MO dye (λ_{peak} = 460 nm). This parameter may have a significant contribution to the low activity during the photocatalytic tests for the RhB dye (λ_{peak} = 554 nm).

It is important to note that due to the relatively low light flux (15 mW m^{-2}) and the wavelength specific to the excitation of the semiconductor ($<$ 530 nm), of WLEDs, using in the photocatalytic reactions improved the photocatalytic performance of Ag_3PO_4 during the reaction cycles by providing a significant reduction in the photocorrosion of Ag_3PO_4.
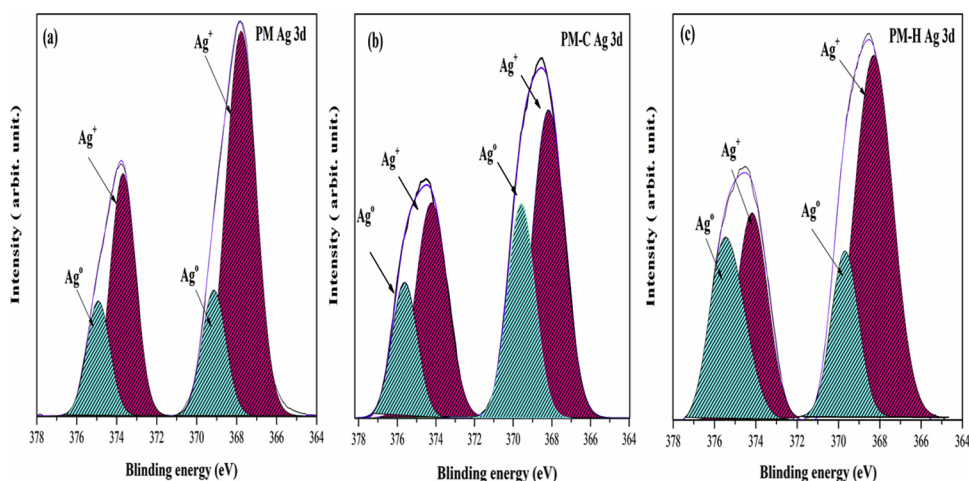
Fig. 8. High-resolution XPS spectra of Ag3d region of (a) PM, (b) PM-C and (c) PM-H samples.

In addition, the system assembled for the development of the photocatalytic assay has important characteristics that differs from conventional photocatalytic reactors which are: (i) the homogeneity relative of the radiation (the reactor is located in the region of highest incidence of light emitted by the WLEDs 98–100% of relative incident radiation) (Fig. S4) and the desired emission spectrum on the surface of the photocatalyst experimentally obtained (Fig. S5), (ii) relatively compact (20 cm x 15 cm), (iii) the small distance between the source and the catalytic reactor (7 cm), (iv) the low heat production that the WELDs produce compared to conventional sources, as well as a reduction in energy consumption during the operating time of the device.

The apparent quantum efficiencies (ϕ_x) of the PM, PM-C, and PM-H samples shown in Fig. 12 were determined from the known photon flux value through the reactor, and were obtained using salt of the Parker actinometer.

The results of the apparent quantum efficiency data (Fig. 12a) justify the trend in photocatalytic cycles, as observed in Fig. 11. The PM sample, we observed an increase of 37% and 3% in catalytic efficiency during the second photocatalytic cycle of OM and RhB. As this sample contained no Ag^0, the increase in photocatalytic activity during the second cycle can be attributed to the plasmonic effect of Ag^0, which may have formed during the first catalytic cycle, dispersed on the surface of the catalyst. [8].

However, this yield provided by the Ag/Ag_3PO_4 heterojunction is below that observed for the PM-C sample. Thus, it is possible to conclude the contribution of the oxygen vacancies in the improvement of

the photocatalytic activity of the sample PM-C in relation to the other samples in the degradation of the dyes [89]. In addition, oxygen vacancies may form a local state below the conduction band of Ag_3PO_4, leading to the narrowing of Eg(as confirmed by DRS UV–vis), thus increasing the response of visible light.

Once irradiated under visible light, most electrons can jump from the valence band to the local state formed by the oxygen vacancies in the bulk, leaving the h^+ in the valence band. During the photocatalytic reaction process, defects and oxygen vacancies formed can capture photo-induced electrons, and then the recombination of electrons and photo-induced holes can be effectively inhibited [110], leading to increased photocatalytic activity.

The electrons transported to a surface of the photocatalyst reacted with the biradical, $*O_2*$, dissolved in the solution, forming the superoxide radical anion($*O_2^-$) that along with the hole (h^+), are considered the main oxidant species in heterogeneous photocatalysis processes in which Ag_3PO_4 as an active catalytic site [108,111]. However, both h^+ and $*O_2^-$ can participate in reactions, giving rise to hydroxyl radicals ($*OH$), which can also act on photodegradation of organic pollutants [112].

It is also important to note the effect of the stability that the PM-C sample holds for the photocatalytic cycles of the RhB dye. The Ag^0 on the surface of the Ag_3PO_4 subjected to the calcination method plays an important role in increasing the photocatalytic stability. This is because Ag^0 can serve as a good electron acceptor, which facilitates the rapid electron transfer by inhibiting the reduction of the Ag^+ ion present in
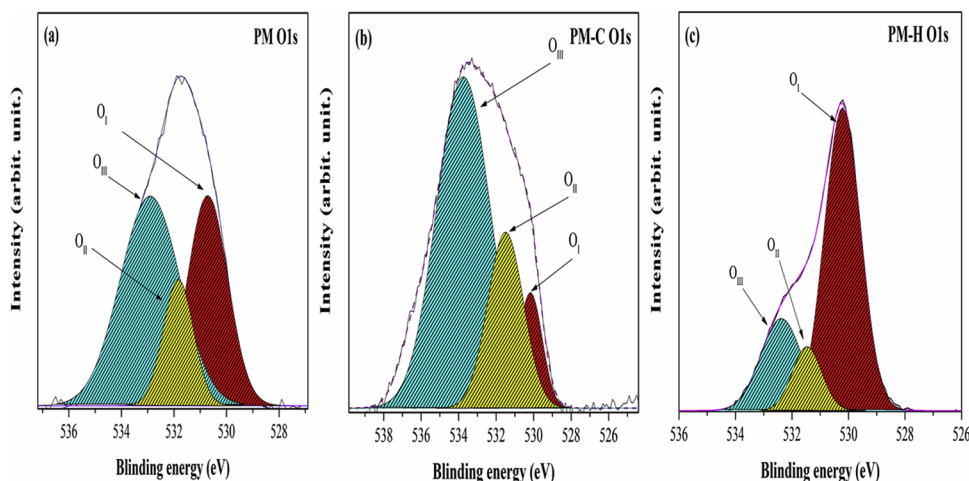

Fig. 9. High-resolution XPS spectra of O1s region of (a) PM, (b) PM-C and (c) PM-H samples.
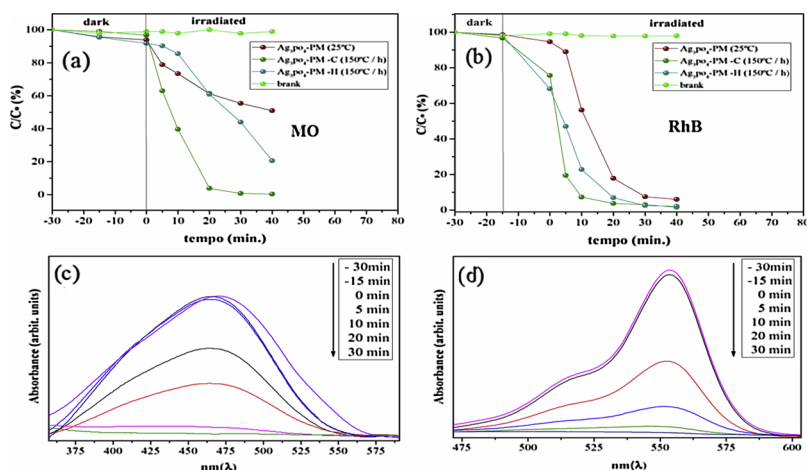
Fig. 10. Photocatalytic degradation curves and photolysis of the MO (10 mg L^{-1}) (a) and RhB(10 mg L^{-1}) samples: PM, PM-C and PM-H, variations in the absorbance of the organic dyes solution (c) MO and (d) RhB in the presence of the PM-C sample irradiated under WLEDs light at different times.
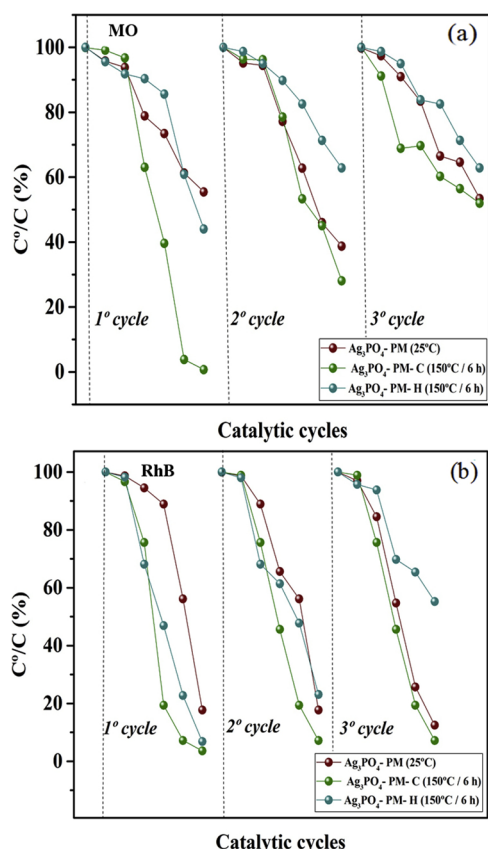

Fig. 11. Photocatalytic cycles of PM, PM-C and PM-H in photodegradation of OM (a) and RhB (b) dyes under WLEDs irradiation.

Fig. 12. Apparent quantum efficiency of samples PM, PM-C and PM-H in degradation of dye MO (a) and RhB (b).

the crystalline network of Ag$_3$PO$_4$ during the cycles [45,96,113].

As reported in recent work of our research group [114], the excess of Ag° and Ag$_2$O generated during the photocorrosion process compromises the catalytic efficiency of the photocatalyst during the catalytic process. However, it can be verified by the apparent quantum efficiency (Fig. 12), especially for the RhB dye that the light source and even at a distance relatively close to the photocatalytic reactor (6 cm) contributed relatively to the delay of the photocorrosion of Ag$_3$PO$_4$ during the cycle's catalysts.

Important to emphasize that the relatively low values of ϕ_x are caused by two factors: (i) calculations were made assuming that dye
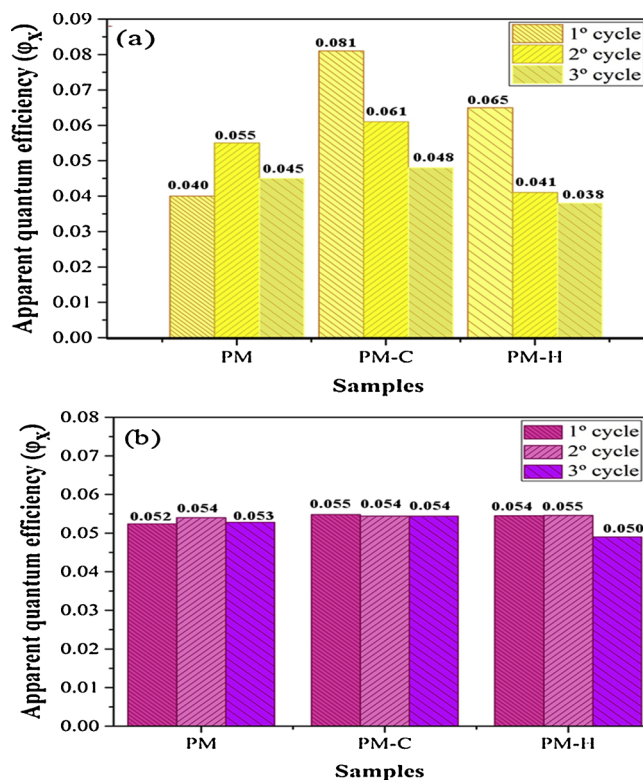
degradation is a process where only one e$^-$/h$^+$ pair effectively degrades, even though, during the process, a large number of carrier entities participate in the complex dye photodegradation mechanism; and (ii) the method does not take into account the fraction of light absorbed by the catalyst in the presence of dye in the solution [115].

4. Conclusion

From the results of microstructural analysis together with the photocatalytic activity results, it was evident that PM-C showed the best photocatalytic response among the synthesized samples owing to the sintering effect during the thermal treatment of the sample at 150 °C for 6 h. This effect contributed to the reduction of the crystallite size and increase in oxygen vacancies and microstructural defects on the surface

of the sample, facilitating the separation, transfer of charges, and low recombination fraction, while allowing the formation of active sites under the surface of the photocatalyst. Moreover, during the photocatalytic assay, we observed the contribution of Ag NPs to the photocatalytic performance of the synthesized samples highlight the sample PM-C. The use the compact photoreator based on white light emitting diode (WLEDs) arrangement was presented as an efficient alternative as it contributed to the low energy consumption and high efficiency of the photocatalytic reactions while delaying the sharp effect of photocorrosion on Ag_3PO_4 sub-microcrystals during the catalytic cycles. In addition, we observed that the adsorption of the dyes under the surface of the catalyst and the effect of light absorption by the substrate for specific wavelengths are important photocatalytic activity parameters.

Acknowledgments

Appendix A. Supplementary data

Supplementary material related to this article can be found, in the online version, at doi:https://doi.org/10.1016/j.jphotochem.2019.03.031.

References

[1] N.I.P. Ayu, E. Kartini, L.D. Prayogi, M. Faisal, Supardi, crystal structure analysis of Li_3PO_4 powder prepared by wet chemical reaction and solid-state reaction by using X-ray diffraction (XRD), Ionics 22 (7) (2016) 1051–1057, https://doi.org/10.1007/s11581-016-1643-z.

[2] A. Hooper, P. McGeehin, K.T. Harrison, B.C. Tofield, Ionic conductivity of pure and doped Na3PO4, J. Solid State Chem. 24 (3) (1978) 265–275, https://doi.org/10.1016/0022-4596(78)90018-X.

[3] V. Najdanovic-Visak, N.J. Lopes, P.Z. Visak, J. Trindade, P.L. Rebelo, Salting-out in aqueous solutions of ionic liquids and K_3PO_4: aqueous biphasic systems and salt precipitation, Int. J. Mol. Sci. 8 (8) (2007), https://doi.org/10.3390/i8080736.

[4] F.H. Firsching, Precipitation of silver phosphate from homogenous solution, Anal. Chem. 33 (7) (1961) 873–874, https://doi.org/10.1021/ac60175a018.

[5] P. Amornpitoksuk, K. Intarasuwan, S. Suwanboon, J. Baltrusaitis, Effect of phosphate salts (Na3PO4, Na2HPO4, and NaH2PO4) on Ag_3PO_4 morphology for photocatalytic dye degradation under visible light and toxicity of the degraded dye products, Ind. Eng. Chem. Res. 52 (49) (2013) 17369–17375, https://doi.org/10.1021/ie401821w.

[6] U. Sulaeman, X. Wu, B. Liu, S. Yin, T. Sato, Synthesis of Ag_3PO_4-polyvinyl alcohol hybrid microcrystal with enhanced visible light photocatalytic activity, Appl. Surf. Sci. 356 (2015) 226–231, https://doi.org/10.1016/j.apsusc.2015.08.067.

[7] J. Chen, X. Yang, C. Zhu, X. Xie, C. Lin, Y. Zhao, Q. Yan, A research on shape-controllable synthesis of Ag_3PO_4/AgBr and its degradation of ciprofloxacin, Water Sci. Technol. 77 (5) (2018) 1230, https://doi.org/10.2166/wst.2017.643.

[8] K. Huang, Y. Lv, W. Zhang, S. Sun, B. Yang, F. Chi, S. Ran, X. Liu, O_4/Ag photocatalyst with visible-light photocatalytic activity, Mater. Res. 18 (2015) 939–945, https://doi.org/10.1590/1516-1439.346614.

[9] L. Huang, S.H.U. Yin, C. Guo, Y. Huang, M. Wang, Q. Dong, H. Li, T. Kimura, M. Tanaka, T. Sato, Oleate-assisted room temperature synthesis and high photocatalytic activity of Ag_3PO_4 nanoparticles for no decomposition, Funct. Mater. Lett. 05 (02) (2012) 1260005, https://doi.org/10.1142/S1793604712600053.

[10] X. Yan, Q. Gao, J. Qin, X. Yang, Y. Li, H. Tang, Morphology-controlled synthesis of Ag_3PO_4 microcubes with enhanced visible-light-driven photocatalytic activity, Ceram. Int. 39 (8) (2013) 9715–9720, https://doi.org/10.1016/j.ceramint.2013.04.044.

[11] H. Wang, L. He, L. Wang, L. Pengfei, L. Guo, X. Han, J. Li, Facile Synthesis of Ag_3PO_4 Tetrapod Microcrystals with an Increased Percentage of Exposed {110} Facets and Highly Efficient Photocatalytic Properties, (2012), https://doi.org/10.1039/C2CE26366A.

[12] J. Wang, F. Teng, M. Chen, J. Xu, Y. Song, X. Zhou, Facile synthesis of novel Ag_3PO_4 tetrapods and the {110} facets-dominated photocatalytic activity, CrystEngComm 15 (1) (2013) 39–42, https://doi.org/10.1039/C2CE26060C.

[13] Y. Bi, S. Ouyang, N. Umezawa, J. Cao, J. Ye, Facet effect of single-crystalline Ag_3PO_4 sub-microcrystals on photocatalytic properties, J. Am. Chem. Soc. 133 (17) (2011) 6490–6492, https://doi.org/10.1021/ja2002132.

[14] H.N. Ng, C. Calvo, R. Faggiani, A new investigation of the structure of silver orthophosphate, Acta Crystallogr. Sect. B 34 (3) (1978) 898–899, https://doi.org/10.1107/S0567740878014570.

[15] G. Botelho, J.C. Sczancoski, J. Andres, L. Gracia, E. Longo, Experimental and

[16] A. Kunz, P. Peralta-Zamora, S.Gd. Moraes, N. Durán, New tendencies on textile effluent treatment, Química Nova 25 (2002) 78–82, https://doi.org/10.1590/S0100-40422002000100014.

[17] D.A. Bright, W.T. Dushenko, S.L. Grundy, K.J. Reimer, Evidence for short-range transport of polychlorinated biphenyls in the Canadian Arctic using congener signatures of PCBs in soils, Sci. Total Environ. 160–161 (1995) 251–263, https://doi.org/10.1016/0048-9697(95)04361-4.

[18] M.A. Al-Ghouti, M.A.M. Khraisheh, S.J. Allen, M.N. Ahmad, The removal of dyes from textile wastewater: a study of the physical characteristics and adsorption mechanisms of diatomaceo us earth, J. Environ. Manage. 69 (3) (2003) 229–238, https://doi.org/10.1016/j.jenvman.2003.09.005.

[19] S.M.A. Guelli U. de Souza, L.C. Peruzzo, A.A. Ulson de Souza, Numerical study of the adsorption of dyes from textile effluents, Appl. Math. Model. 32 (9) (2008) 1711–1718, https://doi.org/10.1016/j.apm.2007.06.007.

[20] M.M. Araújo, L.K.R. Silva, J.C. Sczancoski, M.O. Orlandi, E. Longo, A.G.D. Santos, J.L.S. Sá, R.S. Santos, G.E. Luz, L.S. Cavalcante, Anatase TiO_2 nanocrystals anchored at inside of SBA-15 mesopores and their optical behavior, Appl. Surf. Sci. 389 (2016) 1137–1147, https://doi.org/10.1016/j.apsusc.2016.08.018.

[21] E.L.S. Souza, C.J. Dalmaschio, M.G.R. Filho, G. Luz, R.Sd. Santos, E. Longo, J.A. Cabral, Structural Refinement and Photocatalytic Properties of $CuWO_4$ Crystals, (2014), pp. 894–902 https://www.formatex.info/microscopy6/book/894-902.pdf.

[22] I.A. Alaton, I.A. Balcioglu, D.W. Bahnemann, Advanced oxidation of a reactive dyebath effluent: comparison of O_3, H_2O_2/UV-C and TiO_2/UV-A processes, Water Res. 36 (5) (2002) 1143–1154, https://doi.org/10.1016/S0043-1354(01)00335-9.

[23] D.F. Laine, I.F. Cheng, The destruction of organic pollutants under mild reaction conditions: a review, Microchem. J. 85 (2) (2007) 183–193, https://doi.org/10.1016/j.microc.2006.07.002.

[24] F. Martínez, G. Calleja, J.A. Melero, R. Molina, Heterogeneous photo-Fenton degradation of phenolic aqueous solutions over iron-containing SBA-15 catalyst, Appl. Catal. B 60 (3) (2005) 181–190, https://doi.org/10.1016/j.apcatb.2005.03.004.

[25] A. Fujishima, K. Honda, Electrochemical photolysis of water at a semiconductor electrode, Nature 238 (1972) 37, https://doi.org/10.1038/238037a0.

[26] R.T. Asahi, T. Morikawa, T. Ohwaki, K. Aoki, Y. Taga, Visible-light photocatalysis in nitrogen-doped titanium oxides, Science 293 (2001) 269–271, https://doi.org/10.1126/science.1061051.

[27] Z. Zou, J. Ye, K. Sayama, H. Arakawa, Direct splitting of water under visible light irradiation with an oxide semiconductor photocatalyst, Nature 414 (2001) 625, https://doi.org/10.1038/414625a.

[28] A. Kudo, Y. Miseki, Heterogeneous photocatalyst materials for water splitting, Chem. Soc. Rev. 38 (1) (2009) 253–278, https://doi.org/10.1039/B800489G.

[29] C. Chen, W. Ma, J. Zhao, Semiconductor-mediated photodegradation of pollutants under visible-light irradiation, Chem. Soc. Rev. 39 (11) (2010) 4206–4219, https://doi.org/10.1039/B921692H.

[30] H. Tong, S. Ouyang, Y. Bi, N. Umezawa, M. Oshikiri, J. Ye, Nano-photocatalytic materials: possibilities and challenges, Adv. Mater. 24 (2) (2012) 229–251, https://doi.org/10.1002/adma.201102752.

[31] Y. Qu, L. Liao, Y. Li, H. Zhang, Y. Huang, X. Duan, Electrically conductive and optically active porous silicon nanowires, Nano Lett. 9 (12) (2009) 4539–4543, https://doi.org/10.1021/nl903030n.

[32] M.A. Shannon, P.W. Bohn, M. Elimelech, J.G. Georgiadis, B.J. Mariñas, A.M. Mayes, Science and technology for water purification in the coming decades, Nature 452 (2008) 301, https://doi.org/10.1038/nature06599.

[33] X. Lang, X. Chen, J. Zhao, Heterogeneous visible light photocatalysis for selective organic transformations, Chem. Soc. Rev. 43 (1) (2014) 473–486, https://doi.org/10.1039/C3CS60188A.

[34] X. Chen, C. Li, M. Gratzel, R. Kostecki, S.S. Mao, Nanomaterials for renewable energy production and storage, Chem. Soc. Rev. 41 (23) (2012) 7909–7937, https://doi.org/10.1039/C2CS35230C.

[35] Y.P. Xie, G.S. Wang, Visible light responsive porous lanthanum-doped Ag_3PO_4 photocatalyst with high photocatalytic water oxidation activity, J. Colloid Interface Sci. 430 (2014) 1–5, https://doi.org/10.1016/j.jcis.2014.05.020.

[36] K. Dai, L. Lu, C. Liang, G. Zhu, L. Geng, Advance ternary surface-fluorinated TiO_2 nanosheet/Ag_3PO_4/Ag composite photocatalyst with planar heterojunction and island Ag electron capture center, RSC Adv. 4 (107) (2014) 62751–62758, https://doi.org/10.1039/C4RA08899A.

[37] Z. Yi, J. Ye, N. Kikugawa, T. Kako, S. Ouyang, H. Stuart-Williams, H. Yang, J. Cao, W. Luo, Z. Li, Y. Liu, R.L. Withers, An orthophosphate semiconductor with photooxidation properties under visible-light irradiation, Nat. Mater. 9 (2010) 559, https://doi.org/10.1021/jp512111v.

[38] C.-T. Dinh, T.-D. Nguyen, F. Kleitz, T.-O. Do, Large-scale synthesis of uniform silver orthophosphate colloidal nanocrystals exhibiting high visible light photocatalytic activity, Chem. Commun. 47 (27) (2011) 7797–7799, https://doi.org/10.1039/C1CC12014J.

[39] J.J. Liu, X.L. Fu, S.F. Chen, Y.F. Zhu, Electronic structure and optical properties of Ag_3PO_4 photocatalyst calculated by hybrid density functional method, Appl. Phys. Lett. 99 (19) (2011) 191903, https://doi.org/10.1063/1.3660319.

[40] Y.-z. Ma, F. Cheng, W.-s. Liu, J. Wang, Y.-k. Wang, Research progress of Ag_3PO_4-based photocatalyst: fundamentals and performance enhancement, Trans. Nonferrous Met. Soc. China 25 (1) (2015) 112–121, https://doi.org/10.1016/S1003-6326(15)63585-3.

[41] N. Umezawa, O. Shuxin, J. Ye, Theoretical study of high photocatalytic

performance of Ag3PO4, Phys. Rev. B 83 (3) (2011) 035202, https://doi.org/10.1103/PhysRevB.83.035202.

[42] Q. Liang, Y. Shi, W. Ma, Z. Li, X. Yang, Enhanced photocatalytic activity and structural stability by hybridizing Ag3PO4 nanospheres with graphene oxide sheets, J. Chem. Soc. Faraday Trans. 14 (45) (2012) 15657–15665, https://doi.org/10.1039/C2CP42465G.

[43] T.A. Vu, C.D. Dao, T.T.T. Hoang, K.T. Nguyen, G.H. Le, P.T. Dang, H.T.K. Tran, T.V. Nguyen, Highly photocatalytic activity of novel nano-sized Ag3PO4 for Rhodamine B degradation under visible light irradiation, Mater. Lett. 92 (2013) 57–60, https://doi.org/10.1016/j.matlet.2012.10.023.

[44] D.J. Martin, N. Umezawa, X. Chen, J. Ye, J. Tang, Facet engineered Ag3PO4 for efficient water photooxidation, Energy Environ. Sci. 6 (11) (2013) 3380–3386, https://doi.org/10.1039/C3EE42260G.

[45] Y. Liu, L. Fang, H. Lu, L. Liu, H. Wang, C. Hu, Highly efficient and stable Ag/Ag3PO4 plasmonic photocatalyst in visible light, Catal. Commun. 17 (2012) 200–204, https://doi.org/10.1016/j.catcom.2011.11.001.

[46] P. Wang, B. Huang, X. Qin, X. Zhang, Y. Dai, J. Wei, M.-H. Whangbo, Ag@AgCl: a highly efficient and stable photocatalyst active under visible light, Angew. Chemie Int. Ed. 47 (41) (2008) 7931–7933, https://doi.org/10.1002/anie.200802483.

[47] H. Xu, H. Li, J. Xia, S. Yin, Z. Luo, L. Liu, L. Xu, One-pot synthesis of visible-light-driven plasmonic photocatalyst Ag/AgCl in ionic liquid, ACS Appl. Mater. Interfaces 3 (1) (2011) 22–29, https://doi.org/10.1021/am100781n.

[48] X. Guan, J. Shi, L. Guo, Ag3PO4 photocatalyst: hydrothermal preparation and enhanced O2 evolution under visible-light irradiation, Int. J. Hydrogen Energy 38 (27) (2013) 11870–11877, https://doi.org/10.1016/j.ijhydene.2013.07.017.

[49] R. Chong, X. Cheng, B. Wang, D. Li, Z. Chang, L. Zhang, Enhanced photocatalytic activity of Ag3PO4 for oxygen evolution and methylene blue degeneration: effect of calcination temperature, Int. J. Hydrogen Energy 41 (4) (2016) 2575–2582, https://doi.org/10.1016/j.ijhydene.2015.12.061.

[50] J.-W. Xu, Z.-D. Gao, K. Han, Y. Liu, Y.-Y. Song, Synthesis of magnetically separable Ag3PO4/TiO2/Fe3O4 heterostructure with enhanced photocatalytic performance under visible light for photoinactivation of Bacteria, ACS Appl. Mater. Interfaces 6 (17) (2014) 15122–15131, https://doi.org/10.1021/am5032727.

[51] S. Nakamura, S. Pearton, G. Fasol, The Blue Laser Diode: the Complete Story, Springer - Verlag, 2000, p. 368 doi: 10.10.07/978-3-662-04156-7.

[52] N. Shuji, GaN Growth Using GaN Buffer Layer, Jpn. J. Appl. Phys. 30 (10A) (1991) L1705 http://stacks.iop.org/1347-4065/30/i=10A/a=L1705.

[53] C. Casado, R. Timmers, A. Sergejevs, C.T. Clarke, D.W.E. Allsopp, C.R. Bowen, R. van Grieken, J. Marugán, Design and validation of a LED-based high intensity photocatalytic reactor for quantifying activity measurements, Chem. Eng. J. 327 (2017) 1043–1055, https://doi.org/10.1016/j.cej.2017.06.167.

[54] W.-K. Jo, R.J. Tayade, New generation energy-efficient light source for photocatalysis: LEDs for environmental applications, Ind. Eng. Chem. Res. 53 (6) (2014) 2073–2084, https://doi.org/10.1021/ie404176g.

[55] V.K. Khanna, Fundamentals of Solid-State Lighting: LEDs, OLEDs, and Their Applications in Illumination and Displays, CRC Press, 2014 ISBN 9781466561090.

[56] G. Caglioti, A. Paoletti, F.P. Ricci, Choice of collimators for a crystal spectrometer for neutron diffraction, Nucl. Instrum. 3 (4) (1958) 223–228, https://doi.org/10.1016/0369-643X(58)90029-X.

[57] A. Márcio de Lima Batista, M. Miranda, F. Itana Chaves Custódio Martins, C. Morilla Santos, J. Sasaki, Synthesis of Cerium Oxide (CeO2) by Co-precipitation for Application as a Reference Material for X-ray Powder Diffraction Peak Widths, (2018), https://doi.org/10.1017/S0885715617001208.

[58] J. Rodriguez-Carvajal, Recent developments of the program FULLPROF, Newsletter 26 (2001).

[59] P. Stephens, Phenomenological model of anisotropic peak broadening in powder diffraction, J. Appl. Crystallogr. 32 (2) (1999) 281–289, https://doi.org/10.1107/S0021889898006001.

[60] P.P. Kubelka, New contributions to the optics of intensely light-scattering materials. Part I, J. Opt. Soc. Am. 38 (5) (1948) 448–457, https://doi.org/10.1364/JOSA.38.000448.

[61] N.A. Rodríguez, A. Savateev, M.A. Grela, D. Dontsova, Facile synthesis of potassium poly(heptazine imide) (PHIK)/Ti-Based metal–organic framework (MIL-125-NH2) composites for photocatalytic applications, ACS Appl. Mater. Interfaces 9 (27) (2017) 22941–22949, https://doi.org/10.1021/acsami.7b04745.

[62] N. Serpone, Relative photonic efficiencies and quantum yields in heterogeneous photocatalysis, J. Photochem. Photobiol. A: Chem. 104 (1) (1997) 1–12, https://doi.org/10.1016/S1010-6030(96)04538-8.

[63] J.M. Newsam, A.K. Cheetham, B.C. Tofield, Structural studies of the high-temperature modifications of sodium and silver orthophosphates, II-Na3PO4 and II-Ag3PO4, and of the low-temperature form I-Ag3PO4, Solid State Ion. 1 (5) (1980) 377–393, https://doi.org/10.1016/0167-2738(80)90037-5.

[64] B.D. Cullity, Elements of x-ray Diffraction, 2nd ed., Addison-Wesley Publishing Company, 1978.

[65] C.A.M. Casanova, N.M. Balzaretti, G. Voronin, J.A.H. da Jornada, Experimental study of plastic deformation during sintering of cubic boron nitride compacts, Diam. Relat. Mater. 8 (8) (1999) 1451–1454, https://doi.org/10.1016/S0925-9635(99)00057-6.

[66] K. Momma, F. Izumi, VESTA: a three-dimensional visualization system for electronic and structural analysis, J. Appl. Crystallogr. 41 (3) (2008) 653–658, https://doi.org/10.1107/S0021889808012016.

[67] X. Ma, B. Lu, D. Li, R. Shi, C. Pan, Y. Zhu, Origin of photocatalytic activation of silver orthophosphate from first-principles, J. Phys. Chem. C 115 (11) (2011) 4680–4687, https://doi.org/10.1021/jp111167u.

[68] G. Will, Powder Diffraction the Rietveld Method and the Two-stage Method to Determine and Refine Crystal Structures for Powder Diffraction Data, Springer,

Germany, 2006, https://doi.org/10.1007/3-540-27986-5.

[69] D. Balzar, N. Audebrand, M.R. Daymond, A. Fitch, A. Hewat, J.I. Langford, A. Le Bail, D. Louer, O. Masson, C.N. McCowan, N.C. Popa, P.W. Stephens, B.H. Toby, Size-strain line-broadening analysis of the ceria round-robin sample, J. Appl. Crystallogr. 37 (6) (2004) 911–924, https://doi.org/10.1107/S0021889804022551.

[70] D.K. Smith, J. Fiala, E. Ryba, Book reviews - the Rietveld method, young R. A, Powder Diffr. 8 (4) (2013) 252–254, https://doi.org/10.1017/S0885715600019497.

[71] A. Khorsand Zak, W.H.Abd. Majid, M.E. Abrishami, R. Yousefi, X-ray analysis of ZnO nanoparticles by Williamson–Hall and size–strain plot methods, Solid State Sci. 13 (1) (2011) 251–256 doi:10.10.16/j.solidstatesciences.2010.11.024.

[72] A.R. Stokes, A.J.C. Wilson, The diffraction of X rays by distorted crystal aggregates - I, Proc. Phys. Soc. 56 (3) (1944) 174, https://doi.org/10.1088/0959-5309/56/3/303.

[73] T. Ungár, Dislocation model of strain anisotropy, Powder Diffr. 23 (2) (2012) 125–132, https://doi.org/10.1154/1.2918549.

[74] B.E. Warren, X-ray studies of deformed metals, Prog. Met. Phys. 8 (1959) 147–202, https://doi.org/10.1016/0502-8205(59)90015-2.

[75] A. Velea, C.N. Borca, G. Socol, A.C. Galca, D. Grolimund, M. Popescu, J.Av. Bokhoven, In-situ crystallization of GeTe\GaSb phase change memory stacked films, J. Appl. Phys. 116 (23) (2014) 234306, https://doi.org/10.1063/1.4904741.

[76] F. Zaza, G. Orio, E. Serra, F. Caprioli, M. Pasquali, Low-temperature capacitive sensor based on perovskite oxides, AIP Conf. Proc. 1667 (1) (2015) 020004, https://doi.org/10.1063/1.4922560.

[77] I.L. Validžić, M. Mitrić, S.P. Ahrenkiel, M.I. Čomor, Microstructural analysis and the multicolor UV/violet/blue/green/yellow PL observed from the synthesized ZnO nano-leaves and nano-rods, Metall. Mater. Trans. A 46 (8) (2015) 3679–3686, https://doi.org/10.1007/s11661-015-2961-x.

[78] M. Casas-Cabanas, M.R. Palacín, J. Rodríguez-Carvajal, Microstructural analysis of nickel hydroxide: anisotropic size versus stacking faults, Powder Diffr. 20 (4) (2012) 334–344, https://doi.org/10.1154/1.2137340.

[79] W. Schatt, M. Hinz, On the Generalizability of Defect-activated Sintering, (1988).

[80] J.E. Burke, Role of grain boundaries in sintering, J. Am. Ceram. Soc. 40 (3) (1957) 80–85, https://doi.org/10.1111/j.1151-2916.1957.tb12580.x.

[81] R. Krause, W. Schatt, B. Vetter, A. Polity, Study of sintering processes in copper and nickel by positron annihilation, Cryst. Res. Technol. 25 (7) (1990) 819–825 doi:10.10.02/crat.2170250715.

[82] G.C. Kuczynski, Self-diffusion in sintering of metallic particles, in: S. Sōmiya, Y. Moriyoshi (Eds.), Sintering Key Papers, Springer Netherlands, Dordrecht, 1990, pp. 509–527 doi: 10.10.07/978-94-009-0741-6_33.

[83] P. Cd. Sousa Filho, O.A. Serra, Liquid phase synthesis methodologies for the obtainment of rare earth-based inorganic nanomaterials, Química Nova 38 (2015) 679–696 http://quimicanova.sbq.org.br/detalhe_artigo.asp?id=6215.

[84] R.S. Winburn, D.G. Grier, G.J. McCarthy, R.B. Peterson, Rietveld quantitative X-ray diffraction analysis of NIST fly ash standard reference materials, Powder Diffr. 15 (3) (2013) 163–172, https://doi.org/10.1017/S0885715600011015.

[85] A. Gualtieri, G. Artioli, Quantitative determination of chrysotile asbestos in bulk materials by combined Rietveld and RIR methods, Powder Diffr. 10 (4) (2013) 269–277, https://doi.org/10.1017/S0885715600014962.

[86] R. Snellings, A. Salze, K.L. Scrivener, Use of X-ray diffraction to quantify amorphous supplementary cementitious materials in anhydrous and hydrated blended cements, Cem. Concr. Res. 64 (2014) 89–98, https://doi.org/10.1016/j.cemconres.2014.06.011.

[87] R. Chong, X. Cheng, B. Wang, D. Li, Z. Chang, L. Zhang, Enhanced photocatalytic activity of Ag3PO4 for oxygen evolution and methylene blue degeneration: effect of calcination temperature, Int. J. Hydrogen Energy 41 (4) (2016) 2575–2582, https://doi.org/10.1016/j.ijhydene.2015.12.061.

[88] C.G. Kontoyannis, N.V. Vagenas, Calcium carbonate phase analysis using XRD and FT-Raman spectroscopy, Analyst 125 (2) (2000) 251–255, https://doi.org/10.1039/A908609I.

[89] P. Dong, G. Hou, C. Liu, X. Zhang, H. Tian, F. Xu, X. Xi, R. Shao, Origin of activity and stability enhancement for Ag3PO photocatalyst after calcination, Materials 9 (12) (2016) 968, https://doi.org/10.3390/ma9120968.

[90] C.M. Preston, W.A. Adams, A laser Raman spectroscopic study of aqueous orthophosphate salts, J. Phys. Chem. 83 (7) (1979) 814–821, https://doi.org/10.1021/j100470a011.

[91] H. Wang, Y. Bai, J. Yang, X. Lang, J. Li, L. Guo, A facile way to rejuvenate Ag3PO4 as a recyclable highly efficient photocatalyst, Chem. Eur. J. 18 (18) (2012) 5524–5529, https://doi.org/10.1002/chem.201103189.

[92] Q. Liang, Y. Shi, W. Ma, Z. Li, X. Yang, Enhanced Photocatalytic Activity and Structural Stability by Hybridizing Ag3PO Nanospheres with Graphene Oxide Sheets, (2012), https://doi.org/10.1039/C2CP42465G.

[93] Y.M. Moustafa, K. El-Egili, Infrared spectra of sodium phosphate glasses, J. Non. Solids 240 (1) (1998) 144–153, https://doi.org/10.1016/S0022-3093(98)00711-X.

[94] Z. Hua Chun, Ostwald ripening: a synthetic approach for hollow nanomaterials, Curr. Nanosci. 3 (2) (2007) 177–181, https://doi.org/10.2174/157341307780619279.

[95] S.T. Gentry, S.F. Kendra, M.W. Bezpalko, Ostwald ripening in metallic nanoparticles: stochastic kinetics, J. Phys. Chem. C 115 (26) (2011) 12736–12741, https://doi.org/10.1021/jp2009786.

[96] Y. Bi, H. Hu, S. Ouyang, Z. Jiao, G. Lu, J. Ye, Selective growth of Ag3PO submicrocubes on Ag nanowires to fabricate necklace-like heterostructures for photocatalytic applications, J. Mater. Chem. 22 (30) (2012) 14847–14850, https://doi.

org/10.1039/C2JM32800C.

[97] H. Tan, Z. Zhao, W.-b. Zhu, E.N. Coker, B. Li, M. Zheng, W. Yu, H. Fan, Z. Sun, Oxygen vacancy enhanced photocatalytic activity of pervoskite $SrTiO_3$, ACS Appl. Mater. Interfaces 6 (21) (2014) 19184–19190, https://doi.org/10.1021/am5051907.

[98] E. Forgacs, T. Cserháti, G. Oros, Removal of synthetic dyes from wastewaters: a review, Environ. Int. 30 (7) (2004) 953–971, https://doi.org/10.1016/j.envint.2004.02.001.

[99] D. Gouzie, R.P. Dodd, D.M. White, Dye-tracing studies in southwestern Missouri, USA: indication of stratigraphic flow control in the burlington limestone, Hydrogeol. J. 18 (4) (2010) 1043–1052, https://doi.org/10.1007/s10040-010-0581-5.

[100] J.S. Jang, H.G. Kim, J.S. Lee, Heterojunction semiconductors: a strategy to develop efficient photocatalytic materials for visible light water splitting, Catal. Today 185 (1) (2012) 270–277, https://doi.org/10.1016/j.cattod.2011.07.008.

[101] S.K. Pardeshi, A.B. Patil, Effect of morphology and crystallite size on solar photocatalytic activity of zinc oxide synthesized by solution free mechanochemical method, J. Mol. Catal. A Chem. 308 (1) (2009) 32–40, https://doi.org/10.1016/j.molcata.2009.03.023.

[102] O. Vasile, E. Andronescu, C. Ghiţulică, B. Vasile, E. Vasile, Grain size effect on photocatalytic properties of nanocrystalline ZnO, UPB Sci. Bull. Ser. B: Chem. Mater. Sci. 76 (2) (2014) 3-12. ISSN 1454 – 2331.

[103] H.-S. Chin, L.-S. Chao, The effect of thermal annealing processes on structural and photoluminescence of zinc oxide thin film, J. Nanomater. 2013 (2013) 8, https://doi.org/10.1155/2013/424953.

[104] M.M. Pariona, S.A. Pianaro, Diffusion simulation of zinc and oxygen, and analysis of the varistor durability of ZnO using the factorial design, Cermica 46 (2000) 145–151, https://doi.org/10.1590/S0366-69132000000300005.

[105] P.J.B. Marcos, D. Gouvêa, Effect of MgO segregation and solubilization on the morphology of ZrO_2 powders during synthesis by the Pechini's method, Cermica 50 (2004) 38–42, https://doi.org/10.1590/S0366-69132004000100006.

[106] M. Kong, Y. Li, X. Chen, T. Tian, P. Fang, F. Zheng, X. Zhao, Tuning the relative concentration ratio of bulk defects to surface defects in TiO_2 nanocrystals leads to high photocatalytic efficiency, J. Am. Chem. Soc. 133 (41) (2011) 16414–16417,

https://doi.org/10.1021/ja207826q.

[107] J. Zhuang, W. Dai, Q. Tian, Z. Li, L. Xie, J. Wang, P. Liu, X. Shi, D. Wang, Photocatalytic degradation of RhB over TiO_2 bilayer films: effect of defects and their location, Langmuir 26 (12) (2010) 9686–9694, https://doi.org/10.1021/la100302m.

[108] W. Wang, B. Cheng, J. Yu, G. Liu, W. Fan, Visible-light photocatalytic activity and deactivation mechanism of Ag_3PO spherical particles, Chem. Asian J. 7 (8) (2012) 1902–1908, https://doi.org/10.1002/asia.201200197.

[109] W. Wang, B. Cheng, J. Yu, G. Liu, W. Fan, Visible-light photocatalytic activity and deactivation mechanism of Ag3PO4 spherical particles, Chem. Asian J. 7 (8) (2012) 1902–1908.

[110] J. Liqiang, S. Xiaojun, X. Baifu, W. Baiqi, C. Weimin, F. Honggang, The preparation and characterization of La doped TiO_2 nanoparticles and their photocatalytic activity, J. Solid State Chem. 177 (10) (2004) 3375–3382, https://doi.org/10.1016/j.jssc.2004.05.064.

[111] J. Ren, Y. Chai, Q. Liu, L. Zhang, W.-L. Dai, Intercorrelated Ag_3PO nanoparticles decorated with graphic carbon nitride: enhanced stability and photocatalytic activities for water treatment, Appl. Surf. Sci. 403 (2017) 177–186, https://doi.org/10.1016/j.apsusc.2017.01.172.

[112] Y. Chai, L. Wang, J. Ren, W.-L. Dai, A novel visible light-driven Ag_3PO/SBA-15 nanocomposite: preparation and application in the photo-degradation of pollutants, Appl. Surf. Sci. 324 (2015) 212–220, https://doi.org/10.1016/j.apsusc.2014.09.207.

[113] Y. Liu, L. Fang, H. Lu, Y. Li, C. Hu, H. Yu, One-pot pyridine-assisted synthesis of visible-light-driven photocatalyst Ag/Ag_3PO, Appl. Catal. B 115–116 (2012) 245–252, https://doi.org/10.1016/j.apcatb.2011.12.038.

[114] T.M.S. Costa, M.S. Lima, J.F. Cruz Filho, L.J. Silva, R.S. Santos, G.E. Luz, Synthesis, characterization, and photocatalytic activity of Ag3PO4/SBA-15 in ciprofloxacin degradation under polychromatic irradiation, J. Photochem. Photobiol. A: Chem. 364 (2018) 461–471.

[115] J.M. Buriak, P.V. Kamat, K.S. Schanze, Best practices for reporting on heterogeneous photocatalysis, ACS Appl. Mater. Interfaces 6 (15) (2014) 11815–11816, https://doi.org/10.1021/am504389z.